

NASA TECHNICAL NOTE



NASA TN D-5492

NASA TN D-5492

19980819 154

EXPERIMENTAL INVESTIGATION
OF THE MOMENTUM TRANSFER
ASSOCIATED WITH IMPACT INTO
THIN ALUMINUM TARGETS

PLEASE RETURN TO:

by C. Robert Nysmith and B. Pat Denardo
Ames Research Center
Moffett Field, Calif.

BMD TECHNICAL INFORMATION CENTER
BALLISTIC MISSILE DEFENSE ORGANIZATION
7100 DEFENSE PENTAGON
WASHINGTON D.C. 20301-7100

U100711

1. Report No. NASA TN D-5492		2. Government Accession No.		3. Recipient's Catalog No.	
4. Title and Subtitle EXPERIMENTAL INVESTIGATION OF THE MOMENTUM TRANSFER ASSOCIATED WITH IMPACT INTO THIN ALUMINUM TARGETS				5. Report Date October 1969	
				6. Performing Organization Code	
7. Author(s) C. Robert Nysmith and B. Pat Denardo				8. Performing Organization Report No. A-3252	
9. Performing Organization Name and Address NASA Ames Research Center Moffett Field, Calif. 94035				10. Work Unit No. 124-09-15-02-00-21	
				11. Contract or Grant No.	
12. Sponsoring Agency Name and Address National Aeronautics and Space Administration Washington, D. C. 20546				13. Type of Report and Period Covered Technical Note	
				14. Sponsoring Agency Code	
15. Supplementary Notes					
16. Abstract <p>Aluminum spheres of 3.2-mm diameter were fired into thin 2024-T3 aluminum targets at velocities to 8.1 km/sec, and the axial components of the ejecta and target momenta were measured.</p> <p>It was observed that the momentum transfer associated with impacts into thin targets can be classified into four different impact phases; these phases reflect differing physical processes in the targets, and are determined by the impact velocity and the target thickness. The physical processes are described and the momentum data within each impact phase are correlated. Measurements of target mass loss, minimum hole diameter, and threshold-spallation velocity were also obtained and are reported.</p>					
17. Key Words Suggested by Authors hypervelocity impact momentum transfer impact phases meteor bumpers				18. Distribution Statement Unclassified - Unlimited	
19. Security Classif. (of this report) Unclassified		20. Security Classif. (of this page) Unclassified		21. No. of Pages 16	
				22. Price* \$ 3.00	

*For sale by the Clearinghouse for Federal Scientific and Technical Information
Springfield, Virginia 22151

EXPERIMENTAL INVESTIGATION OF THE MOMENTUM TRANSFER
ASSOCIATED WITH IMPACT INTO THIN ALUMINUM TARGETS

By C. Robert Nysmith and B. Pat Denardo

Ames Research Center

SUMMARY

Aluminum spheres of 3.2-mm diameter were fired into thin 2024-T3 aluminum targets at velocities to 8.1 km/sec, and the axial components of the ejecta and target momenta were measured.

It was observed that the momentum transfer associated with impacts into thin targets can be classified into four different impact phases; these phases reflect differing physical processes in the targets, and are determined by the impact velocity and the target thickness. The physical processes are described and the momentum data within each impact phase are correlated. Measurements of target mass loss, minimum hole diameter, and threshold-spallation velocity were also obtained and are reported.

INTRODUCTION

The use of meteor bumpers on spacecraft to minimize the damage from the impact of meteoric debris was first proposed in 1947 by Whipple (ref. 1), who suggested that part of the meteoroid and bumper material would be vaporized and fragmented upon impact and the kinetic energy of the meteoroid divided among the broken meteoroid and bumper fragments. The structure behind the bumper would then be more resistant to penetration by the smaller, lower-energy individual particles sprayed over a large area. This hypothesis has been verified by experimental impact tests of meteor bumpers (refs. 2, 3, and 4).

Despite much additional study, however, bumper performance is not fundamentally well understood, and an optimum (minimum weight) design cannot be defined for even the simplest bumper-hull structure (double wall). The problem is further complicated when other structural and environmental requirements dictate the use of more complex structures. Laboratory impact tests of these sophisticated structures give results that can be used for a qualitative evaluation of a particular structure within the experimental range of velocities but provide no information for improved designs. At the present time, there is no proven design method for a given meteoroid environment; a great deal of information on bumper and structural component performance is needed before the results can be extrapolated to the meteoroid environment.

Since meteor bumper effectiveness is determined by the damage to the structure behind the bumper, investigations of the physical properties (momentum, particle size, particle state, and particle distribution) of the material emanating from the rear of the bumper can be used to evaluate bumper performance. In addition, once the properties of the bumper spray material are known, the tests can be extended to an investigation of individual structural components so that, eventually, an optimum bumper-hull structure can be designed on the basis of the known performance of each structural component.

In this regard, a number of investigators are concerned with determining the momentum of the bumper spray material as a function of the varying impact conditions. Some of these results are given in references 5, 6, and 7. A similar program of research directed toward determining the momentum imparted by a projectile to the various components of a spacecraft structure is being conducted at Ames Research Center. The present report provides data defining the momentum imparted to a bumper and the resulting impulse that must be absorbed by the structure behind the bumper. The primary test variables are the projectile velocity and the bumper thickness. Other related data are presented, such as bumper mass loss, bumper hole diameter, and the bumper threshold-spallation velocity.

SYMBOLS

c, c_1, c_2	proportionality parameters in ejecta momentum equation (9)
D	average minimum hole diameter, mm
d	diameter of projectile, mm
k	correlating factor in spray momentum equation
ΔM	target mass loss, g
m	mass of projectile, g
$(MV)_E$	momentum of target ejecta, kg-m/sec
$(MV)_S$	momentum of target spray, kg-m/sec
$(MT)_T$	momentum of target, kg-m/sec
t	thickness of target, mm
v	impact velocity, km/sec
v_0	velocity at which the onset of mass ejection occurs, km/sec
v_z	front-surface spallation velocity, km/sec

v_s	apparent threshold spallation velocity, km/sec
$v_{s(\text{actual})}$	actual threshold spallation velocity, km/sec
ϵ	target ductility, elongation, cm/cm
ρ_p	projectile density, g/cc
ρ_T	target density, g/cc

EXPERIMENTAL PROCEDURE

Tests were conducted by launching small projectiles from the light-gas gun of the Ames Research Center Impact Range into various bumper targets at velocities to 8.1 km/sec. The range configuration is illustrated in figure 1, and the gun is described in detail in reference 8.

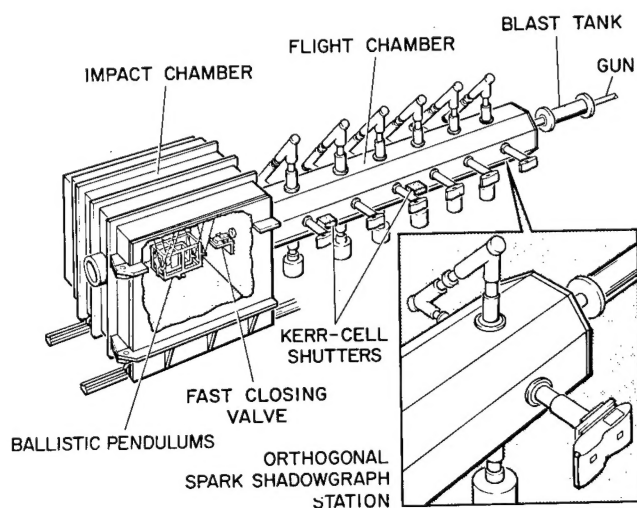


Figure 1.- Range configuration.

The projectiles were 3.2-mm-diameter 2017-T4 aluminum spheres with a nominal mass of 0.046 g. They were carried down the bore of the gun barrel in sabots that protected them from the propellant gases. After launch, the sabots separated aerodynamically and were deflected in the blast-tank portion of the range to prevent them from impacting the targets. The pressure in the range varied from test to test between 35 to 180 mm Hg of nitrogen depending on the launch conditions and the impact velocity required.

The spheres passed through a 3.5-m-long flight chamber instrumented with six spark shadowgraph stations, each representing two orthogonal views of the projectile in flight. Two of the stations were equipped with Kerr-cell shutters with exposure times of about 5 nsec so that the structural integrity of the model could be accurately determined. Intervals of time were recorded on 10- and 100-mc counter chronographs, and the measurements of time and distance permitted the determination of projectile velocity to an accuracy of 0.5 percent.

From the flight chamber, the projectiles entered the instrumented impact chamber through a valved port. The valve, actuated by a signal from one of the uprange shadowgraph stations, closed within 0.5 msec after passage of the projectile, thereby protecting the target from the gun blast and other disturbances. Tare tests with the valve indicated that neither the valve movement nor gun blast influenced the impact tests. In addition, inspection of all targets and test equipment after each test in this

investigation showed no evidence of extraneous damage, and it was concluded that the fast-closing valve effectively isolated the target setup from events in the rest of the range.

The targets were single 150-mm square sheets of 2024-T3 aluminum ranging in thickness from 1.00 mm to 12.5 mm. They were rigidly mounted to the target pendulum of the multiple ballistic pendulum system shown in figure 2. A second pendulum was arranged to catch the ejecta material thrown uprange from the impact. The pendulums were mounted within one another but were independently suspended using classical five-wire suspension systems and could swing without interference. Thus, the ejecta pendulum measured the axial momentum imparted by the material thrown uprange from the target face in the form of target ejecta, and the target pendulum measured the axial momentum experienced by the bumper. Since the momenta to be measured, in many cases, were quite small, the pendulums were made of aluminum channel so that they would be as light as possible and still be structurally rigid. Each pendulum was weighed accurately and its period determined before each test. During each test an open-shutter camera recorded the motion of a steady light attached to each pendulum. Pendulum velocity, and hence momentum, was determined by the method outlined in reference 9. An analysis of all the parameters involved in the computation of pendulum momentum indicates that momenta were determined to within an accuracy of 1 percent.

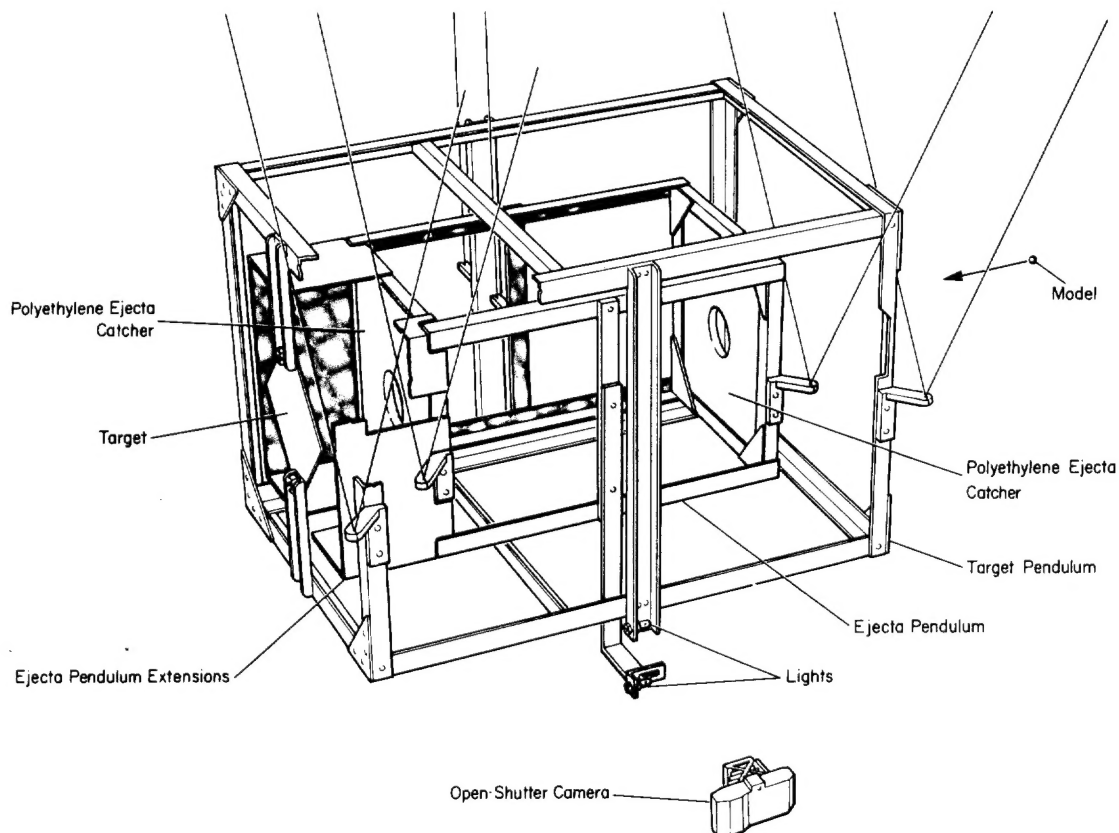


Figure 2.- Multiple ballistic pendulum system.

The selection of the material to be used on the ejecta pendulum to catch the ejecta was very critical: If this material tended to splash material back when the ejecta struck it, the secondary backsplash affected the target pendulum and made the results of both measurements unreliable. After a short investigation of the cratering characteristics of a number of materials, high-density polyethylene was selected as a catcher material because of its ability to resist splashing.

Two 12.5-mm-thick slabs of polyethylene were attached to the front and rear of the ejecta pendulum, as shown in figure 2. A 25.5-mm diameter hole, centered on boreline, was drilled through each polyethylene slab so that the projectile could pass through the ejecta pendulum and strike the target. The polyethylene slab nearest the target served as the ejecta catcher, and the polyethylene on the front of the ejecta pendulum served a dual purpose as a counterweight and as a backup to catch any ejecta that passed through the hole in the polyethylene on the rear of the pendulum. Since the targets in this investigation were generally thin and were perforated by impact, material was ejected at relatively low angles to the target surface. To catch all of the target ejecta, it was necessary to position the rearmost polyethylene slab as close to the target as possible while maintaining enough clearance so that sufficient pendulum motions could be obtained for accurate momentum measurements. This separation distance was approximately 76 mm. In addition, thin-walled metal extensions were attached to the rear of the ejecta pendulum that projected downrange and essentially surrounded the target. These extensions, shown in figure 2, ensured that any axial momentum contribution from ejecta leaving almost parallel to the target face would not be lost. Inspection of the polyethylene slab after each test showed a well-defined ejecta damage pattern that clearly indicated whether any ejecta passed through the hole in the polyethylene.

A number of tests were also conducted in which a third pendulum was used to catch the spray material and measure its axial momentum. However, regardless of the design of the spray catcher and the material used to catch the spray, the spray material was always so energetic that backsplash occurred and reliable momenta measurements could not be obtained. Therefore, attempts to experimentally measure the momentum of the spray material were abandoned.

DISCUSSION OF RESULTS

General Remarks on Momentum Transfer in Thin Targets

When a projectile impacts a target, the projectile momentum must be conserved in the target ejecta, target spray, and target motion. These quantities are related through the conservation-of-momentum equation

$$mv = (MV)_T + (MV)_S - (MV)_E \quad (1)$$

where the projectile, target, and spray momenta are positive measured down-range and the ejecta momentum is positive measured uprange. Three of these terms (mv , $(MV)_T$, and $(MV)_E$) were measured in the present experiments making it possible to calculate the fourth, $(MV)_S$.

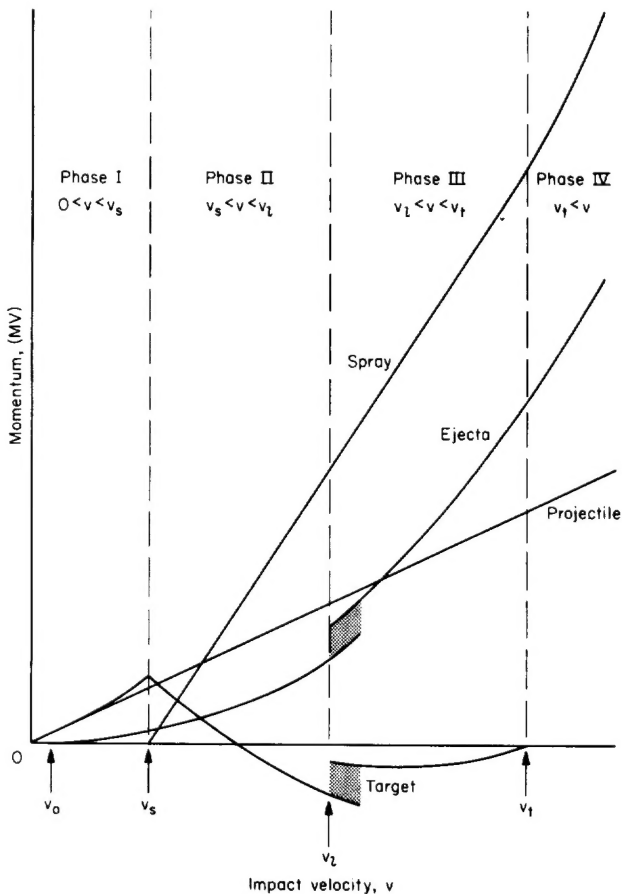


Figure 3.- Representation of the division of momentum for a typical t/d ratio.

Momentum and the ejecta momentum. Momentum data for semi-infinitely thick targets such as that presented and discussed in references 9 and 10 are defined by this phase. For thin-target investigations, as the targets approach the thick-target limit, the momentum results should move toward agreement with the published thick-target data.

Phase II.- At the threshold spallation velocity, v_s , material is spalled from the rear of the target and the spray momentum increases from zero. The target momentum accordingly begins to decrease. For certain t/d , as the impact velocity increases from v_s , the target momentum actually becomes negative as shown in figure 3. This implies that, under certain conditions, the impulsive load on the meteor bumper of a space vehicle will be directed away from the vehicle hull rather than toward it.

Phase III.- As the impact velocity increases throughout the Phase II impact region, all the components of momentum vary in a smooth and systematic fashion. Then a transition velocity v_l is attained, at which target material is spalled from the target's front surface causing an increase in both

Division of axial momentum depends on the physical processes in the target during impact. A generalized representation of the division of momentum for a typical t/d is shown in figure 3, where the various momentum components are plotted versus impact velocity. This representation has four impact velocity phases, described below. Note that the actual results of tests for a particular t/d may fall into a more limited number of phases because of the velocity limitations of the test facility. Thus, data within all four target reaction phases were obtained by testing at a number of t/d over as large a velocity range as possible.

Phase I.- Within the Phase I region, the target has not been perforated or spalled, $(MV)_S = 0$, and equation (1) reduces to

$$(MV)_T = mv + (MV)_E \quad (2)$$

Thus, the momentum of the target is simply the sum of the projectile

the ejecta and target momentum. This phenomenon is not related to the crater lip detachment process described by Denardo (ref. 11); it appears instead to be a thin-target front-surface-spallation process caused by interactions of the reflected shock waves within the target material. The shaded region in figure 3 indicates that this spallation process does not always occur at precisely v_L and is not always complete. In practice, for a given t/d , there is a small velocity range (which has not been determined) in which front-surface spallation is quite random. This spallation phenomenon represents the impact velocity range within which a given target becomes essentially thin in that its front and rear surfaces after impact are virtually identical in appearance. As the impact velocity increases above v_L , the target momentum gradually approaches zero.

Phase IV.- Within the Phase IV region, the target momentum is zero and equation (1) reduces to

$$(MV)_S = mv + (MV)_E \quad (3)$$

This impact region is represented by very thin targets impacted at the velocities of these tests or thicker targets impacted at much higher velocities.

Correlation of Momentum Data

In the following discussion, the various components of momentum are expressed as functions of velocity and t/d . These relations do not include any effects of projectile size since a constant diameter projectile was used throughout this test series. The projectile diameter is used throughout this paper as a normalization factor for the target thickness, and the results given here do not imply the absence of a scale effect such as that observed in reference 11. The extent of the scale effect has yet to be determined.

Spray momentum.- In figure 4 the spray momentum, calculated from the measurements by use of equation (1), is plotted versus the impact velocity for the various t/d . The data are fitted by equations of the form

$$(MV)_S = mk(v - v_S) \quad (4)$$

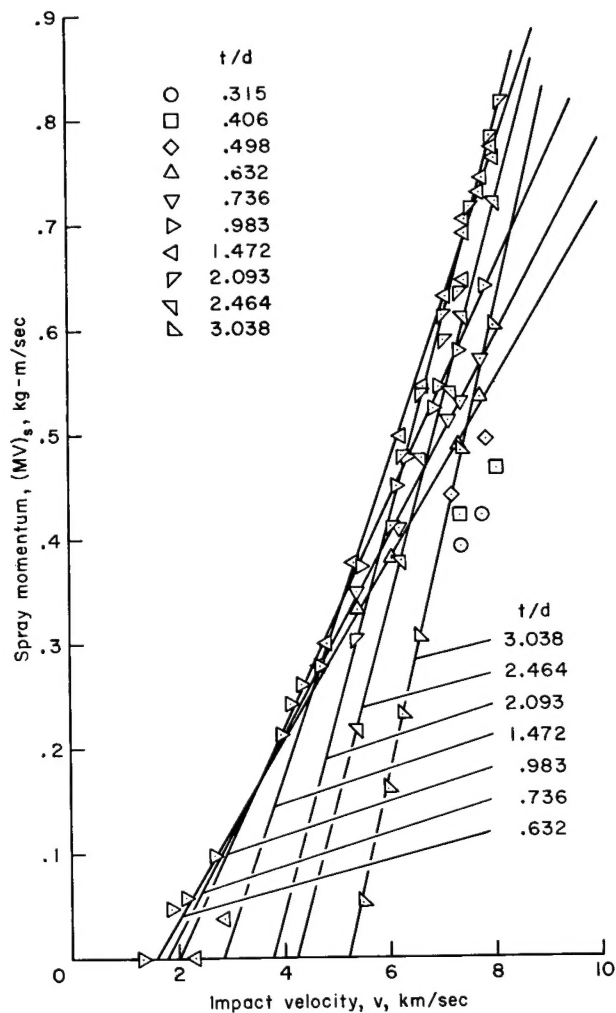


Figure 4.- Variation of spray momentum with impact velocity for various t/d ratios.

where both k , the slope of a particular curve, and v_s , the intercept of the curve with the velocity axis, are functions of t/d .

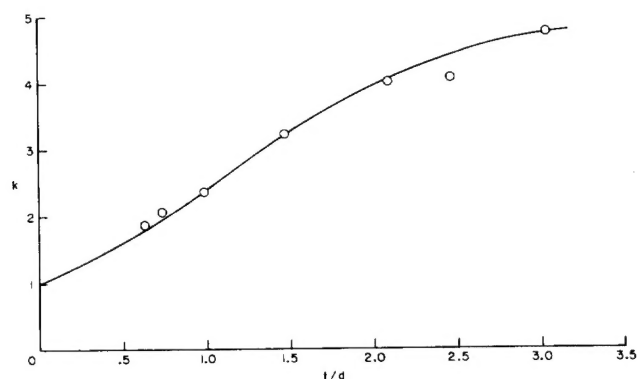


Figure 5.- Variation of k with t/d .

For each t/d greater than 0.498, least-squares values for k and v_s are plotted versus t/d in figures 5 and 6, respectively. In the limit of very thin targets, k must go to 1.0 and v_s must go to zero so that $(MV)_s = mv$ (spray momentum equals projectile momentum).

In figure 6, the threshold velocity curve, as determined from the intercepts of the linear spray momentum curves with the velocity axis in figure 4, is given by the equation

$$v_s = 2.08(t/d)^{0.83} \quad (5)$$

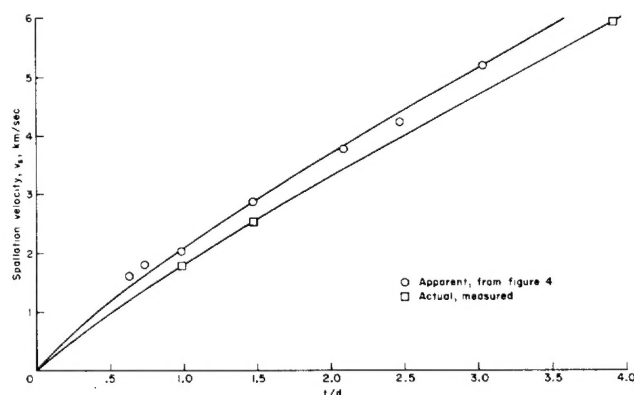


Figure 6.- Variation of the spallation velocity with t/d .

However, as explained in the next section, the momentum measurements of targets at velocities near the threshold spallation velocity indicate that a small velocity range is required for the spray momentum curves to become linear. Consequently, the actual threshold spallation velocities are always somewhat less than those given by equation (5).

Actual threshold spallation velocity.- A short test series was conducted to determine the actual thresh-

hold spallation velocities for three target thicknesses. The targets were tested at velocities both greater than and less than the threshold condition, and the threshold spallation velocity was determined within ± 0.06 km/sec for each target thickness. These data are presented in figure 6 and are fit by the equation

$$v_{s(\text{actual})} = 1.80(t/d)^{7/8} \quad (6)$$

Equations (5) and (6) are limited to the impact of 2024-T3 aluminum targets by 3.2-mm-diameter aluminum spheres. These equations may be applicable to other projectile sizes and materials and other "brittle" target materials if they are adjusted on the basis of the results of references 11 and 12. With appropriate adjustments to equation (6), the actual threshold spallation thickness for other sizes and brittle target materials is predicted to be

$$t/d = 0.44(1/\epsilon)^{1/18}(\rho_P/\rho_T)^{1/2}v^{8/7}d^{1/18} \quad (7)$$

In contrast, Fish (ref. 12) has shown that a ductile target spalls and is perforated at about the same velocity. The threshold spallation thickness for ductile targets is given by the Fish-Summers threshold penetration equation that is based on the data of references 11 and 12:

$$t/d = 0.57(1/\epsilon)^{1/18}(\rho_p/\rho_T)^{1/2}v^{7/8}d^{1/18} \quad (8)$$

Ejecta momentum.— The measurements of ejecta momentum are plotted versus impact velocity for the various t/d in figure 7. These data are fitted by the equation

$$(MV)_E = mc(v - v_0)^2 \quad (9)$$

where c is, once again, a function of t/d and v_0 is the velocity at which the onset of uprange mass ejection occurs. For impacts of identical 2017-T4 aluminum projectiles into thick aluminum targets, Denardo in reference 10 gives v_0 equal to 0.55 km/sec.

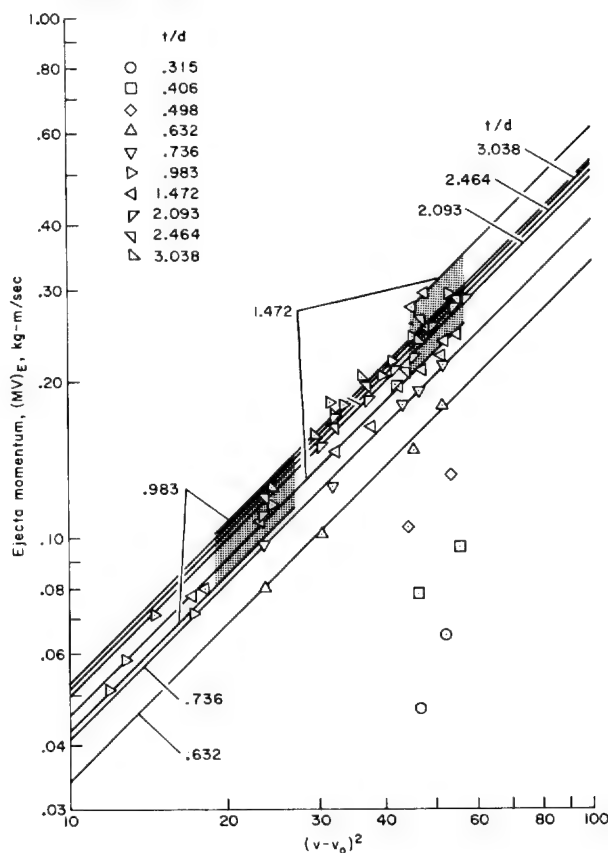


Figure 7.— Variation of ejecta momentum with impact velocity for various t/d ratios.

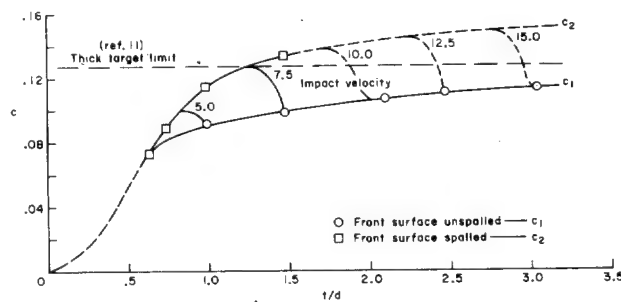
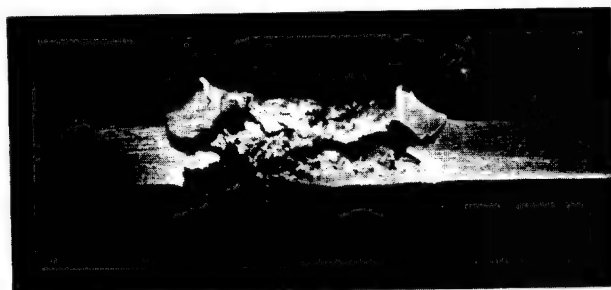
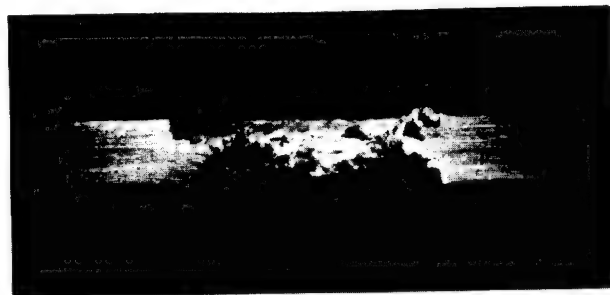


Figure 8.— Variation of c with t/d .

Least-squares values of c , computed for each t/d in figure 7 greater than 0.498, are plotted versus t/d in figure 8. It is observed that c is double-valued for t/d of 0.983 and 1.472. This result is the consequence of the front-surface spallation transition described earlier and represents the transition from impacts in the Phase II region to impacts in the Phase III region. The photographs of targets with and without front-surface spallation in figure 9 illustrate this phenomenon. The difference between the two targets is obvious. The ejecta momentum and, correspondingly, the target momentum are strongly dependent on whether the front surface has spalled. The targets and their corresponding ejecta momenta were consistent in all cases, indicating that within the velocity range of these tests, targets with t/d less than 0.983 are in the "spalled" Phases III and IV impact regions, and targets with t/d greater than 1.472 are in the "no spall" Phase I and II impact regions. Targets with t/d of 0.983 and 1.472 encompass the transition region



(a) Front surface not spalled.



(b) Front surface spalled.

Figure 9.- Illustration of target front surface spallation phenomenon for $t/d = 1.472$ and $v = 7.50$ km/sec.

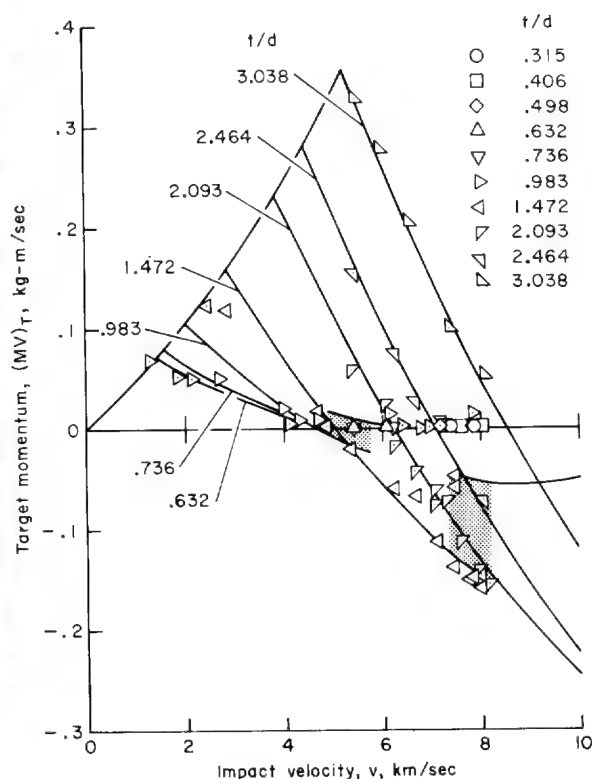


Figure 10.- Variation of target momentum with impact velocity for various t/d ratios.

between Phases II and III and give an approximation for the front-surface spallation velocity v_L , such that

$$v_L \approx 5(t/d) \quad (10)$$

It may be noticed that the constant in this equation is very nearly the sonic velocity in aluminum. It seems reasonable that spallation from the front surface will be some function of the sonic velocity, but the data of these tests are too limited to determine this relation.

In figure 8, the front-surface spall curve has been extrapolated to the larger t/d of this experiment, and correspondingly higher impact velocities based upon the ejecta momentum data for a t/d of 1.472. Velocity curves, calculated from equation (10), representing the impact velocity at which front-surface spallation occurs and the ejecta momentum changes, are also presented. The horizontal dashed curve represents the value of c that fits the data presented in references 10 and 11 for semi-infinitely thick targets. Values of c_1 , that is, values of c for targets where the front surface has not spalled, should approach this value in the limit of large t/d .

Target momentum.- Figure 10 presents the target momentum as a function of the impact velocity for the different t/d . This figure clearly shows the target response for the various phases on impact. For t/d of 0.983 and less, the target momentum is zero or becomes zero within the velocity range of these tests. This denotes the Phase IV impact region. Within this region, the spray momentum is given by equation (3),

$$(MV)_S = mv + (MV)_E \quad (3)$$

Substituting equation (9) into equation (3) gives

$$(MV)_S = mv + cm(v - v_0)^2 \quad (11)$$

within the Phase IV region.

Summary of Momentum Data

The various momentum equations used to correlate the data throughout the four impact phases, and the transition velocities for each phase are summarized below.

Phase I: The target has not been perforated or spalled.

$$(MV)_S = 0$$

$$(MV)_E = mc_1(v - v_0)^2$$

$$(MV)_T = mv + mc_1(v - v_0)^2$$

where c_1 is the value of c when the front surface has not spalled and is a function of t/d in figure 8.

Phase II: At v_s , material is spalled from the rear of the target.

$$v_{s(\text{actual})} = 1.80(t/d)^{7/8}$$

$$v_s = 2.08(t/d)^{0.83}$$

$$(MV)_S = mk(v - v_s)$$

$$(MV)_E = mc_1(v - v_0)^2$$

$$(MV)_T = mv + mc_1(v - v_0)^2 - mk(v - v_s)$$

where k is a function of t/d in figure 5.

Phase III: At v_l , material is spalled from the front surface of the target, and the value of c changes from c_1 to c_2 and is also given as a function of t/d in figure 8.

$$v_l \approx 5.0(t/d)$$

$$(MV)_S = mk(v - v_s)$$

$$(MV)_E = mc_2(v - v_0)^2$$

$$(MV)_T = mv + mc_2(v - v_0)^2 - mk(v - v_s)$$

Within this impact region, the target momentum gradually approaches zero.

Phase IV: In this impact region, the target momentum is zero, and the impacts are in every sense thin-target impacts.

$$(MV)_S = mv + mc_2(v - v_0)^2$$

$$(MV)_E = mc_2(v - v_0)^2$$

$$(MV)_T = 0$$

Target Hole Formation and Mass Loss

The average minimum hole diameter in the targets is presented in figure 11, where the ratio of the hole diameter to the projectile diameter, D/d , is plotted versus the impact velocity for the different t/d investigated.¹ All the data for t/d less than 0.983 and the higher velocity points of 0.983 are fitted by the family of curves shown as solid lines and given by the equation

$$D/d = 1.47(t/d)^{0.45}v^{1/2} \quad (12)$$

Equation (12) represents the equilibrium hole growth condition for thin targets impacted at high velocities where front and rear surface effects are negligible and the hole diameter increases primarily as a result of the radially expanding shock wave in the thin sheet. Targets with t/d greater than 0.983 still experience the surface effects characteristic of thick targets and have not attained the equilibrium condition within this velocity range. This reasoning is supported by the fact that only targets with t/d of 0.983 or less were in the Phase IV impact region characteristic of truly thin-target impacts.

Equation (12) and the hole-diameter equation for 2024-T3 aluminum targets impacted by pyrex glass spheres (eq. (2), in ref. 4) differ only by their constant. Provided this change in constants results from the change in projectile density, a postulated equation for the hole diameter produced in 2024-T3 aluminum bumpers by the impact of spherical projectiles (disregarding any projectile size effects) is given by

$$D/d = 0.88\rho_p^{1/2}(t/d)^{0.45}v^{1/2} \quad (13)$$

¹Figures 11 and 12 show more data points than appear in previous momentum-velocity plots. Target hole diameter and mass-loss data were accrued on a number of tests when momentum results were not obtained: during the development phase of the pendulum design and later when malfunction in the pendulum system occurred.

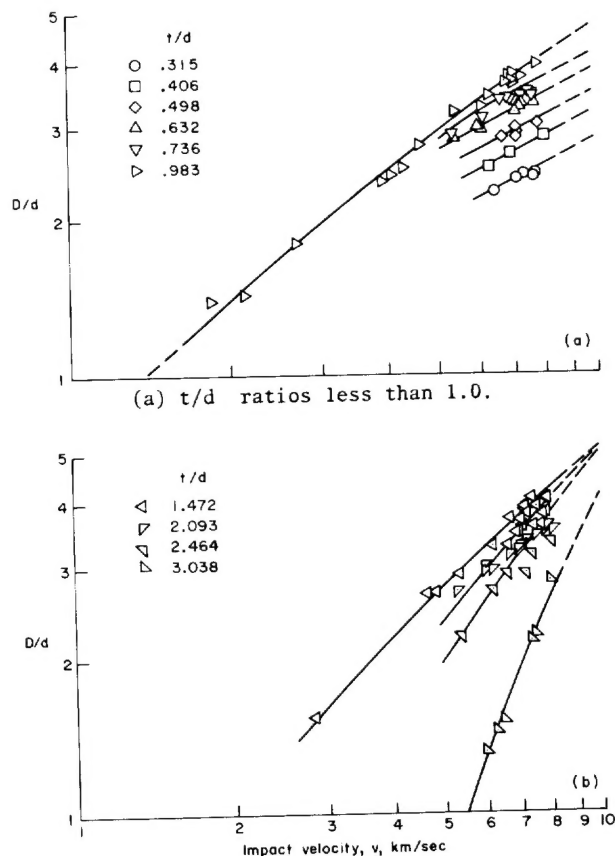


Figure 11.- Variation of hole diameter with impact velocity for various t/d ratios.

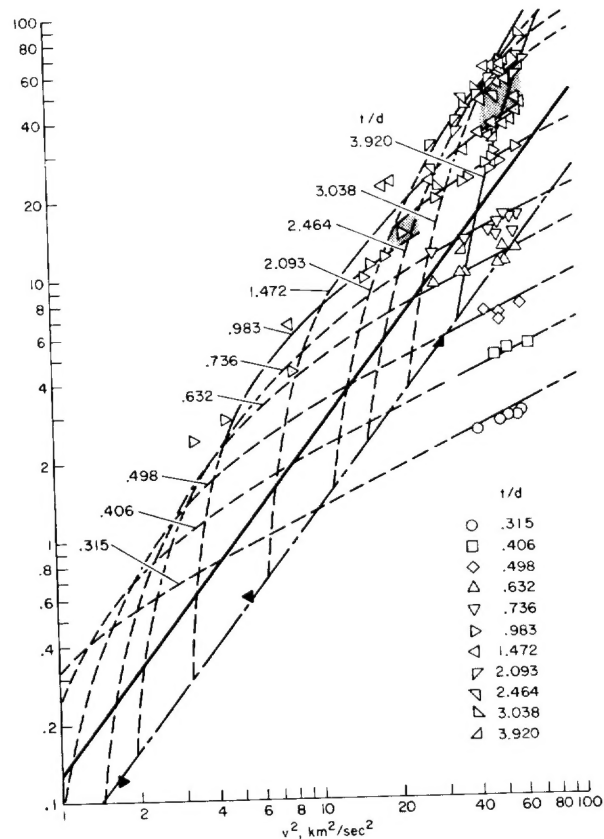


Figure 12.- Variation of target mass loss with impact velocity and t/d ratio.

Measurements also were made of the target mass loss. Each target was weighed before and after it was impacted, and the mass loss was determined to an accuracy of 1 percent or better. These data are presented in figure 12, where the ratio of the target mass loss to the projectile mass, $\Delta M/m$, is plotted versus the impact velocity squared for various t/d . The heavy black curve in this figure represents the thick-target mass-loss data of references 10 and 11 given by

$$\Delta M/m = 0.130v^{2.6} \quad (14)$$

The thin targets that have not spalled or been perforated are shown as the filled symbols and fit the equation

$$\Delta M/m = 0.065v^{2.6} \quad (15)$$

This equation is shown as the dot-dash curve and falls below the thick-target mass-loss curve. One explanation for this result is that some of the projectile's energy is used to deform the thin target and dimple its rear surface rather than eject target mass. It is noted that the mass loss of an unspalled thin target is just half that of a thick target impacted at the same velocity.

The mass-loss data for t/d less than 0.983 and the higher velocity points for 0.983 are fitted by the equation

$$\Delta M/m = 4.1(t/d)^2 v \quad (16)$$

As in the case of the target-hole diameter data, targets with t/d greater than 0.983 have not attained the hole growth equilibrium condition representative of truly thin targets within the velocity range of these tests.

The mass loss of targets of a given thickness can be categorized into the different impact velocity phases in the same manner as the target momentum response.

Phase I: At impact velocities less than the spallation velocity v_s , target mass loss varies according to equation (15).

Phase II: At v_s , the target spalls and the mass loss increases dramatically; as the impact velocity increases above v_s , the target mass loss continues to increase rapidly.

Phase III: At v_l , front-surface spallation occurs and the target mass loss increases abruptly; this phenomenon is illustrated in figure 12 by the mass-loss data for a t/d ratio of 1.472 at an impact velocity of about 7.5 km/sec. Within this impact phase, target mass loss increases slowly with increasing impact velocity since the thin-target equilibrium condition is being approached.

Phase IV: The thin-target equilibrium condition is established, and target mass loss varies according to equation (16).

Equation (16) is identical to equation (3), reference 4, which describes the impact of pyrex glass spheres into thin 2024-T3 aluminum targets, and indicates that target mass loss is independent of projectile density. Target mass loss varies with the square of the hole diameter times the sheet thickness and the projectile and target densities according to

$$\Delta M/m \propto \rho_T D^2 t / \rho_P d^3 = (\rho_T / \rho_P) (D/d)^2 (t/d) \quad (17)$$

Substituting equation (13) into equation (17) yields

$$\Delta M/m \propto \rho_T / \rho_P (\rho_P) (t/d)^{1.9} v = \rho_T (t/d)^{1.9} v \quad (18)$$

Thus, the fact that target mass loss does not vary with projectile density tends to substantiate the target hole diameter dependence on the one-half power of the projectile density. It is also evident that the target hole diameter and mass-loss data are compatible with regard to the impact velocity exponent, but that the target mass loss is influenced by an additional

$(t/d)^{1/10}$ effect. It is thought that this effect is due to additional mass contained in the spalled material that is not accounted for by minimum hole diameter measurements.

Ames Research Center
National Aeronautics and Space Administration
Moffett Field, Calif., 94035, July 7, 1969

REFERENCES

1. Whipple, Fred L.: Meteorites and Space Travel. Astron. J., no. 1161, Feb. 1947, p. 131.
2. Nysmith, C. Robert; and Summers, James L.: An Experimental Investigation of the Impact Resistance of Double-Sheet Structures at Velocities to 24,000 Feet Per Second. NASA TN D-1431, 1962.
3. Maiden, C. J.; and McMillan, A. R.: An Investigation of the Protection Afforded a Spacecraft by a Thin Shield. AIAA Aerospace Sciences Meeting, New York, Jan. 20-22, 1964. AIAA Preprint No. 64-95.
4. Nysmith, C. Robert: Penetration Resistance of Double-Sheet Structures at Velocities to 8.8 Km/Sec. NASA TN D-4568, 1968.
5. Riney, T. D.; and Heyda, J. R.: Hypervelocity Impact Calculations and Their Correlation with Experiment. General Electric TIS Rep. R64SD64, Sept. 1964.
6. Swift, J. F.; and Prater, Capt. R. F.: Simulation of High Velocity Impacts of Thin Targets. Technical Rep. AFML-TR-68-88, May 1968.
7. Cunningham, Capt. John H.: Momentum Distribution in the Debris Cloud Produced by Hypervelocity Perforation of Thin Plates. Technical Rep. AFML-TR-68-174, July 1968.
8. Denardo, B. Pat: Penetration of Polyethylene Into Semi-Infinite 2024-T351 Aluminum Up to Velocities of 37,000 Feet Per Second. NASA TN D-3369, 1966.
9. Denardo, B. Pat: Measurements of Momentum Transfer From Plastic Projectiles to Massive Aluminum Targets at Speeds Up to 25,600 Feet Per Second. NASA TN D-1210, 1962.
10. Denardo, B. Pat; and Nysmith, C. Robert: Momentum Transfer and Cratering Phenomena Associated with the Impact of Aluminum Spheres Into Thick Aluminum Targets at Velocities to 24,000 Feet Per Second. AGARDograph 87, vol. 1, pp. 389-402, The Fluid Dynamic Aspects of Space Flight. Gordon and Breach Science Publishers, New York, 1964.
11. Denardo, B. Pat; Summers, James L.; Nysmith, C. Robert: Projectile Size Effects on Hypervelocity Impact Craters in Aluminum. NASA TN D-4067, 1967.
12. Fish, Richard H.; and Summers, James L.: The Effect of Material Properties on Threshold Perforation. 7th Hypervelocity Impact Symposium, Tampa, Fla., Nov. 17-19, 1964.